# Fast Preparation of Printable Highly Conductive Polymer Nanocomposites by Thermal Decomposition of Silver Carboxylate and Sintering of Silver Nanoparticles

**Rongwei Zhang, Wei Lin, Kyoung-sik Moon, and C. P. Wong***

School of Materials Science and Engineering, Georgia Institute of Technology, 771 Ferst Drive, Atlanta, Georgia 30332

**ABSTRACT** We show the fast preparation of printable highly conductive polymer nanocomposites for future low-cost electronics. Highly conductive polymer nanocomposites, consisting of an epoxy resin, silver flakes, and incorporated silver nanoparticles, have been prepared by fast sintering between silver flakes and the incorporated silver nanoparticles. The fast sintering is attributed to: 1) the thermal decomposition of silver carboxylate—which is present on the surface of the incorporated silver flakes—to form in situ highly reactive silver nanoparticles; 2) the surface activation of the incorporated silver nanoparticles by the removal of surface residues. As a result, polymer nanocomposites prepared at 230 °C for 5 min, at 260 °C for 10 min, and using a typical lead-free solder reflow process show electrical resistivities of $8.1 \times 10^{-5}$, $6.0 \times 10^{-6}$, and $6.3 \times 10^{-5}$ Ω cm, respectively. The correlation between the rheological properties of the adhesive paste and the noncontact printing process has been discussed. With the optimal rheological properties, the formulated highly viscous pastes (221 mPa s at 2500 $s^{-1}$) can be non-contact-printed into dot arrays with a radius of 130 $\mu$m. The noncontact printable polymer nanocomposites with superior electrical conductivity and fast processing are promising for the future of printed electronics.

**KEYWORDS:** nanocomposite • conductive adhesive • sintering • printable • rheology • interconnect

## 1. INTRODUCTION

The preparation of novel printable conductive materials or inks is essential to providing new solutions to the dramatically increasing need for low cost, high performance, electrically functional devices in printed electronics (1−5). Inkjet printing of conductive silver inks on a substrate followed by sintering of silver nanoparticles (6−10) or thermal decomposition of metallo-organic precusors (11, 12) has been developed as a promising technique for a variety of electronic applications. These applications include the interconnection of circuitry on a printed circuit board and the fabrication of conductive tracks or electrodes for thin-film transistors (TFTs), light-emitting diodes, solar cells, sensors and radio frequency identification (RFID) tags (13−15). However, current commercially available silver conductive ink technologies have unaffordable drawbacks. Silver conductive inks do not offer strong enough adhesion on many substrates for use as an interconnect material or for mechanical reliability in flexible substrates (16, 17). After printing and subsequent sintering, the resulting silver films lack cohesion and tend to crack due to considerable shrinkage (17). Moreover, sintering processes take 10 min (18) or longer (19, 20), limiting commercial applications. To address the drawbacks of silver inks, highly conductive epoxy-based polymer composites with a combination of electrical, mechanical, and adhesive functions are a promising solution for printed electronics. One of the main disadvantages of conventional conductive epoxy-based composites is the relatively high electrical resistivity ($3.5 \times 10^{-4}$ Ω cm), compared with eutectic Sn/Pb solders ($1.5 \times 10^{-5}$ Ω cm) (2, 21, 22). By incorporation of silver nanoparticles with nearly complete decomposition of surface residues at the curing temperature, we have demonstrated the preparation of highly conductive polymer nanocomposites with electrical resistivity of $4.8 \times 10^{-5}$ Ω cm at 180 °C for 60 min (23). However, the trend toward mixed assembly technologies, having components attached with both solder and conductive epoxy-based composites on the same board requires uniformity of the curing profile/solder reflow processes. To obtain maximum device level reliability and reduce the cost, conductive epoxy-based composites are required to be cured in a short duration, and most preferably during the solder reflow process.

Here we describe the preparation of printable highly conductive polymer nanocomposites by fast sintering of silver flakes and silver nanoparticles within a polymer matrix. The thermal behavior of silver flakes and silver nanoparticles has been investigated by thermogravimeteric analysis (TGA), surface-enhanced Raman spectroscopy (SERS) and scanning electron microscopy (SEM). This provides a guideline for the processing temperature for the preparation of highly conductive polymer nanocomposites. At certain temperatures, the thermal decomposition of silver carboxy-

* Corresponding author. Phone: 404-894-8391. Fax: 404-894-9140. E-mail: cp.wong@mse.gatech.edu.
Received for review May 24, 2010 and accepted August 10, 2010

DOI: 10.1021/am100456m

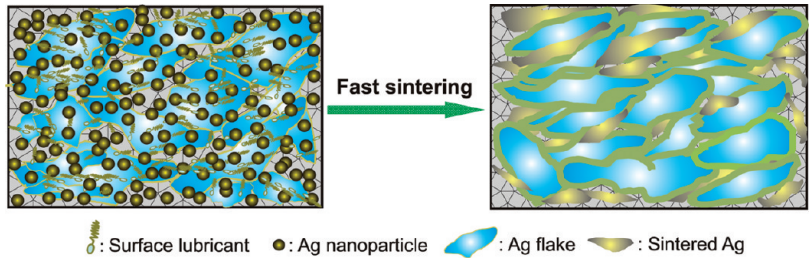


**FIGURE 1. Schematic illustration of the sintering between Ag nanoparticles and Ag flakes within a polymer matrix.**

late on the surface of silver flakes forms highly reactive silver nanoparticles. The formation of silver nanoparticles on the surface of the silver flakes and the thermal decomposition of residues on the surface of the incorporated silver nanoparticles occur simultaneously. Both the in situ formed and the incorporated silver nanoparticles are highly reactive due to their high surface-to-volume ratios and minimal surface residues. The nearly complete decomposition of surface residues facilitates the sintering among silver flakes, in situ formed silver nanoparticles, and the incorporated silver nanoparticles. The sintering process enables the formation of metallurgical bonds between the conductive fillers, instead of physical contacts, within the polymer matrix. The formation of metallurgical bonds effectively reduces or even eliminates the contact resistance among the conductive fillers, leading to highly conductive polymer nanocomposites (Figure 1). The effects of sintering time and temperature on the electrical resistivity of the polymer nanocomposites have been studied. In addition, we discuss the correlation between the rheological properties of conductive adhesive pastes and the noncontact printing process. Finally we demonstrate the noncontact printing of the conductive adhesive pastes.

## 2. EXPERIMENTAL SECTION

Silver nanoparticles used in the present study were synthesized by Combustion Chemical Vapor Condensation (CCVC) method (24−26). Silver flakes with a surface area of 0.57 $m^2/g$ were donated by Ferro Corp. The wide size distribution of silver flakes in the range of several to about twenty micrometers was used to improve the packing density. Typically, surface lubricants such as stearic acid were present on the surface of silver flakes to improve the rheological properties and prevent the aggregation of silver flakes. Silver nanoparticles and silver flakes with an optimized ratio of 4:6 (totally 80 wt % of the mixture) were incorporated into the mixture of diglycidyl ether of bisphenol F (DGEBF, Shell Chemical Co.) and hexahydro-4-methylphthalic anhydride (HMPA, Lindau Chemicals) (21). The weight ratio of DGEBF to HMPA is 1:0.85. The mixture was sonicated for one hour to disperse the conductive fillers within the epoxy resin. Following sonication, the catalyst, 1-cyanoethyl-2-ethyl-4-methylimidazole (2E4MZ-CN, Shikoku Chemicals Corp.), was added into the formulations and the resulting conductive adhesive paste was further sonicated for another 30 min. Two strips of a Kapton tape (Dupont) were applied onto a precleaned glass slide. The formulated paste was printed on the glass slide and put into the oven with a preset temperature for curing. Reflow tests were conducted in a BTU oven (BTU International). The reflow oven has seven chambers and one cooling station. The temperatures for each chamber were set to 75, 110, 156, 198, 221, 255, and 175 °C, characteristic of a typical lead-free solder reflow profile.

After thermal cure or reflow, the bulk resistance ($R$) of polymer composite strips was measured by a Keithley 2000 multimeter. The width and length of the specimen were measured by digital caliper (VWR). The thickness of the specimen was measured by Heidenhain (thickness measuring equipment, ND 281B, Germany). Bulk resistivity, $\rho$, was calculated using eq 1

$$\rho = \frac{tw}{l}R \tag{1}$$

where $l$, $w$, and $t$ are the length, width, and thickness of the sample, respectively. Weight losses of the silver nanoparticles and flakes during heating in air were studied using TGA (TA Instruments, model 2050) at a heating rate of 20 °C/min. Raman spectra of the silver nanoparticles were obtained by using a LabRAM ARAMIS Raman confocal microscope (HORIBA Jobin Yvon) equipped with a 532 nm diode pumped solid state (DPSS) laser. Silicon wafer was used as a substrate for Raman measurements. The rheological properties of the adhesive pastes were measured with cone−plate (2°) geometry at 23 °C by a stress-controlled rheometer from TA Instruments, model AR1000-N. Noncontact printing (or jetting) of the pastes was performed at room temperature by ASM Pacific Technology Ltd. using a jet dispenser with air pressure of 0.1−0.15 bar and jetting time of 5 ms. The nozzle size was 50 $\mu$m.

## 3. RESULTS AND DISCUSSION

**Thermal Decomposition of Silver Carboxylate on the Surface of Silver Flakes.** Commercial silver flakes are generally produced from silver powders by a ball-milling process. To prevent the aggregation of silver powders, an organic lubricant, generally a fatty acid (such as stearic acid), is typically used during the production of silver flakes. After production, a thin layer of lubricant is present on the surface of silver flakes (27−30). The thin layer of lubricant affects the interaction of silver flake with other silver flakes and with the polymer system (29). Consequently, this layer of surface lubricant affects the dispersion of silver flakes, the rheology of formulated pastes, and the electrical conductivity of the resulting polymer composites. Figure 2 shows Raman spectra of the lubricant on the surface of silver flakes without thermal treatment and after isothermal heating at 230, 250, and 260 °C for 5 min. Although the very small shoulder peak at 1700 $cm^{-1}$ indicates the presence of a trace amount of the fatty acid, the peaks at 1432 and 1591 $cm^{-1}$ are assigned to the symmetric ($\nu_s(COO^-)$) and antisymmetric ($\nu_{as}(COO^-)$) stretching vibrations of the carboxylate group, respectively (31−33). The presence of the strong bands due to the stretching vibrations of the carboxylate group and a very weak band due to the

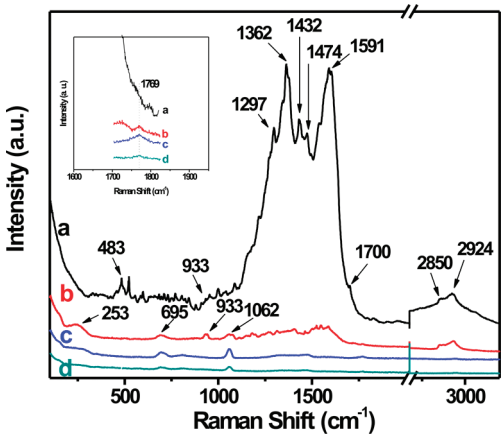


FIGURE 2. Raman spectra of the lubricants on the surface of Ag flakes (a) without thermal treatment and after being isothermally heated at different temperatures for 5 min: (b) 230, (c) 250, and (d) 260 °C.

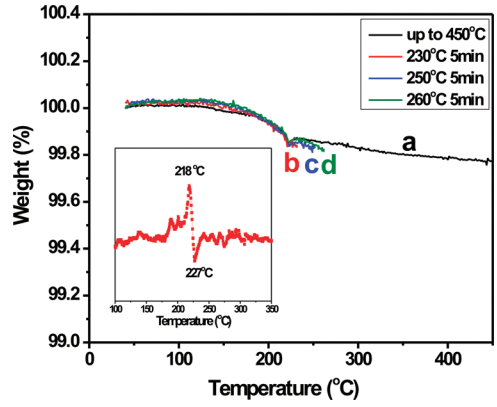


FIGURE 3. TGA of the Ag flakes (a) without thermal treatment and after being isothermally heated at different temperatures for 5 min: (b) 230, (c) 250, and (d) 260 °C. Inset is the first derivative of TGA curve a in the temperature range of 100−350 °C. Significant weight loss and increase are at 218 and 227 °C, respectively.

carbonyl stretching of a carboxylic acid indicates that most fatty acids have been converted into carboxylates on the surface of silver flakes. It is well-known that the binding of fatty acid to a silver surface will lead to the breaking of the O−H bond in the fatty acid and subsequent formation of a carboxylate species, which formed a bond between the oxygen in the carboxylate group and the silver surface (−COOAg) (27−30). Therefore, the thin layer of lubricant is a silver salt formed between fatty acid and silver, i.e., silver carboxylate, rather than a free fatty acid, which is consistent with previous studies (27−30). The peak at 933 $cm^{-1}$ is due to C−$COO^-$ stretching (32). The peaks at 2850 and 2924 $cm^{-1}$ are assigned to the symmetric and asymmetric stretching vibrations of the methylene group. The methylene twisting, wagging and scissor appear at 1297, 1362, and 1474 $cm^{-1}$, respectively (31). Figure 3 shows the TGA results of the silver flakes. A weight loss started at 150 °C and it continued up to 223 °C with a weight loss of 0.14%. This weight loss was followed by a weight increase of 0.01% until 234 °C. The weight increase is due to the oxidation of the lubricant on the silver flakes (27). After 234 °C, further weight loss was observed and final weight loss at 450 °C was 0.23%. The weight loss (0.23%) results from the decomposition of the carboxylate. This amount of the surface lubricant corresponds to roughly a monolayer of stearate on the surface of silver flakes (30). This lubricant monolayer plays a key role in the sintering between silver flakes as it provides an energy barrier for sintering. Substantial removal of the lubricant layer is a prerequisite for sintering to occur. After isothermal heating at 230, 250, and 260 °C for 5 min, the weight losses of the silver flakes are 0.16, 0.17, and 0.18%, respectively. The corresponding Raman spectra of the lubricant on the surface of silver flakes after thermal treatments are shown in Figure 2. The Raman intensities of the lubricant on the surface of the treated silver flakes were significantly reduced. With the thermal treatment at 230 °C, C−C stretching at 1062 $cm^{-1}$, $-COO^-$ deformation at 695 $cm^{-1}$, and Ag−O stretching (−COOAg) at 253 $cm^{-1}$ became prominent, while the peak at 483 $cm^{-1}$ disappeared indicating the decomposition of silver oxide (23, 24). The presence of both the Ag−O stretching and the carboxylate species further indicates that the lubricant layer is silver carboxylate. A Raman peak at 1769 $cm^{-1}$ assigned to C═O stretching appeared after thermal treatment, which further confirmed the oxidation of surface lubricants during the thermal treatment (Figure 2, inset). As the temperature was increased to 250 °C, the peaks at 2924, 2850, and 933 $cm^{-1}$ disappeared and the peak at 253 $cm^{-1}$ showed lower intensity and broadening. Meanwhile, the peak at 1769 $cm^{-1}$ became more obvious, indicating more surface lubricants being oxidized. A further increase in the temperature resulted in the nearly complete disappearance of all peaks except a small peak at 1062 $cm^{-1}$, indicating that most surface lubricants were decomposed. It is well-documented that the thermal decomposition of silver carboxylate leads to the formation of silver nanoparticles (11, 35−40). The thermal decomposition products of silver carboxylate are related to the decomposition atmosphere, heating rate and temperature (37, 39). Studies from Liu et al. reveal that the thermal decomposition product of silver behenate is $CO_2$ at 230 °C, and hydrogen and water at 260 °C, respectively, verified by combined thermogravimetry-differential thermal analysis-mass spectrometry (TG-DTA-MS) analysis (40). In the present study, the thermal decomposition was conducted in air, so the final products were metallic silver and gases ($CO_2$ and $H_2O$) (38, 40). From the TGA and Raman results, it can be concluded that during isothermal heating at the temperatures, the thin layer of lubricant-silver carboxylate-present on the surface of silver flakes has been substantially decomposed, facilitating the sintering between silver flakes.

Figure 4 shows the SEM images of the silver flakes untreated and after isothermal heating at 230, 250, and 260 °C for 5 min. As shown in Figure 4a, the silver flakes have a broad size distribution, which enables higher packing density improving conductivity at given filler loadings. There are some nanosized silver bumps on the surface of untreated silver flakes, but the surface is relatively smooth (Figure 4a, inset). After the thermal treatments, the surface of silver flakes shows increased roughness. The increased surface

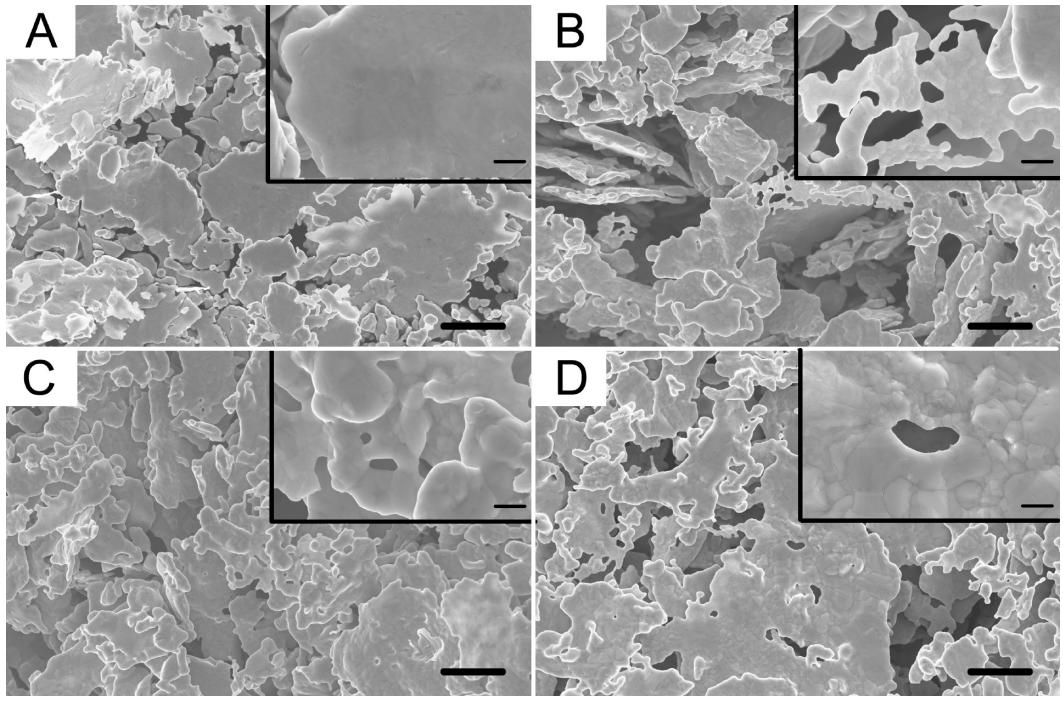


**FIGURE 4. SEM images of the Ag flakes (a) without thermal treatment and after being isothermally heated at different temperatures for 5 min: (b) 230, (c) 250, and (d) 260 °C. Scale bars are 4 $\mu$m and 400 nm (inset), respectively.**

roughness is the result of thermal decomposition of silver carboxylate on the surface of silver flakes, which forms highly reactive nano- or submicrometer-sized silver particles that sintered with the silver flakes (Figure 4b and inset). Note that sintering between adjacent nanosized bumps on the surface of a silver flake is dependent on the decomposition of silver carboxylate since the activation energy of surface diffusion is lower than that of bulk diffusion (41). The lack of a surfactant on the surface of these particles means they have a high surface energy facilitating mass transport, even at temperatures well below the melting temperature of bulk silver (961.8 °C). Sintering of these nanoparticles is evident by the formation of "bridges" between silver flakes after isothermal treatment at 230 °C for 5 min. The higher thermal treatment temperature led to wider necks and rougher surfaces (Figure 4c and inset). As the temperature increases to 260 °C, there was a transition to edge by edge sintering and no isolated flakes were observed at that temperature (Figure 4d and inset). It should be emphasized that during isothermal heating, the thermal decomposition of silver carboxylate to form in situ highly reactive silver nanoparticles is crucial for the sintering between silver flakes, including the sintering between nanosized silver bumps on the surface of silver flakes. Without the thermal decomposition, sintering will not proceed. The formation of "bridge" or edge by edge sintering enables the formation of metallurgical bonds among silver flakes, which remarkably facilitates the electron transport among the silver flakes.

**Thermal Behavior of Silver Nanoparticles.** Nanoparticles tend to sinter or Ostwald ripen to reduce their total free energy (38, 42, 43). Generally, during the synthesis of silver nanoparticles, a variety of stabilizers are utilized to control the size, size distribution and stability (44−47), including long-chain carboxylate (48), polyvinylpyrrodine (49), polyacrylamide (44), and poly(vinyl alcohol) (46). These stabilizers provide an energy barrier to sintering. Sintering occurs only after the substantial removal of the stabilizers. However, the removal of the stabilizers typically requires a temperature higher than 250 °C and a relatively long time because of a relatively large amount of surface residues on the particle surface (>10 wt %) in most cases (47, 49−51), low mobility of surfactants, and the tendency of surfactants to physically adsorb. These surfactants are necessary to obtain a good dispersion and prevent aggregation of silver nanoparticles in the polymer matrix. To address these challenges, we used silver nanoparticles synthesized by CCVC (24−26). Silver nanoparticles synthesized by CCVC offer many significant advantages over those by wet chemical methods for the preparation of highly conductive polymer composites. CCVC nanoparticles synthesis produces nanoparticles whose surface residues have minimal surface coverage and low decomposition temperatures. For example, silver nanoparticles synthesized by CCVC showed a 2.45% weight loss of surface residues at 450 °C; the decomposition of surface residues started at 160 °C and was almost finished at 220 °C (23). Additionally, nanoparticles produced from CCVC methods have narrow size distribution and high production rates (up to 0.1−1 kg/h) (23, 52). Previously, we have found that silver nanoparticles with lower decomposition temperatures of surface residues and lower contents of surface residues are more desirable for low temperature sintering of silver nanoparticles and the preparation of highly conductive polymer composites (23). To facilitate the fast sintering, the experimental conditions for CCVC nanoparticle synthesis were optimized in the present study. Figure 5 shows the TGA results of the silver nanopar-

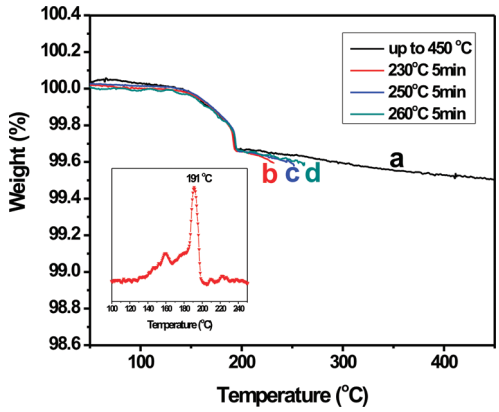


FIGURE 5. TGA of the Ag nanoparticles synthesized by CCVC (a) without thermal treatment and after being isothermally heated at different temperatures for 5 min: (b) 230, (c) 250, and (d) 260 °C. Inset is the first derivative of curve a.

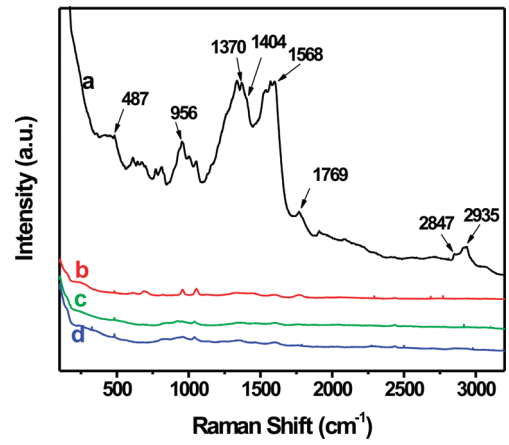


FIGURE 6. Raman spectra of the surface residues on the Ag nanoparticles synthesized by CCVC (a) without a thermal treatment and after being isothermally heated at different temperatures for 5 min: (b) 230, (c) 250, and (d) 260 °C.

ticles. The weight loss of the silver nanoparticles started at 150 °C and was nearly completed at 195 °C. The final weight loss at 450 °C was 0.49%. The present silver nanoparticles with even lower decomposition temperatures of surface residues and lower contents of surface residues will better facilitate the fast sintering between silver nanoparticles and the fast preparation of highly conductive polymer composites. The significant weight loss observed at 191 °C may be attributed to the decomposition of silver oxide or possibly organic residues from the synthesis (23). After isothermal heating at 230, 250, and 260 °C for 5 min, the weight losses of the silver nanoparticles were 0.40, 0.42, and 0.42%, respectively. Comparing the net weight loss of the silver nanoparticles at 450 °C (0.49%), we can conclude that the surface residues have almost been decomposed at these temperatures. The nearly complete decomposition of surface residues at these temperatures within 5 min facilitates the fast sintering of silver nanoparticles. The novel use of CCVC nanoparticles in epoxy-based composites allows the fast preparation of highly conductive polymer nanocomposites.

Raman spectra of the surface residue on silver nanoparticles without thermal treatment and after isothermal heating at 230, 250, and 260 °C for 5 min are shown in Figure 6. The peak at 1769 $cm^{-1}$ assigned to the C═O stretching is related to the oxidation product during the CCVC synthesis under oxidizing conditions. The peaks at 1404 and 1568 $cm^{-1}$ are assigned to the symmetric and antisymmetric stretching vibrations of $-COO^-$ (31−33). The peaks at 2847 and 2935 $cm^{-1}$ are assigned to the symmetric stretching vibrations of the methylene group and the methyl group, respectively. The deformation of the methyl group appears at 1370 $cm^{-1}$. The peak at 956 $cm^{-1}$ is ascribed to the $C-COO^-$ stretching. Additionally, a weak peak centered at 487 $cm^{-1}$ in Figures 3 and 4 indicates the presence of silver oxide on the silver nanoparticle surface. The intensity of the peaks described was significantly reduced after isothermal heating at 230 °C for 5 min. Most of the peaks disappeared after isothermal heating at 250 and 260 °C for 5 min. The disappearance of the peak at 487 $cm^{-1}$ indicated the decomposition of silver oxide at the temperatures. It should be noted that the decomposition temperature of silver oxide varies from 160 to 350 °C (34, 53, 54). Raman results further confirm that the surface residues have almost been decomposed after isothermal heating at the temperatures for 5 min.

Figure 7 shows the SEM images of the silver nanoparticles without thermal treatment and after isothermal heating at 230, 250, and 260 °C for 5 min. Compared with the untreated silver nanoparticles (Figure 7a), the size of the thermally treated silver nanoparticles increased significantly. These nanoparticles formed a porous 3D continuous network after isothermal heating at 230 °C for 5 min (Figure 7b). The formation of necks among the silver nanoparticles was the result of surface diffusion driven by a reduction in surface energy. Surface diffusion dominates at the initial sintering stage since the activation energy of surface diffusion is lower than that of grain boundary and lattice diffusions (41). As the temperature increases to 250 °C, the particle sizes increased further and the necks between them widen (Figure 7c). Densification observed at 260 °C indicates the dominant grain boundary/lattice diffusions during the sintering process (Figure 7d).

**Electrical Properties of Polymer Nanocomposites.** Although the electrical resistivity of silver films close to that of bulk silver ($1.6 \times 10^{-6}$ Ω cm) has been achieved by sintering of silver nanoparticles in silver inks (11, 41, 55), it remains a challenge to sinter silver nanoparticles within polymer matrices to achieve highly conductive polymer composites. In most cases, the incorporation of silver nanoparticles into a polymer matrix results in a polymer composite with a very high resistivity (49, 56, 57), as a result of increased contact points and reduced contact area among conductive fillers (56). The possible reasons are: (1) the difficult debonding or decomposition of organic molecules (or silver oxide) at curing temperatures (6, 23, 58, 59); (2) the impediment of the sintering of silver nanoparticles by high volume fraction (typically 70−80 vol %) of highly cross-linked polymer matrices (23). In the present study, the curing of the epoxy resin and the sintering among the conductive fillers occur simultaneously. Figure 8 shows

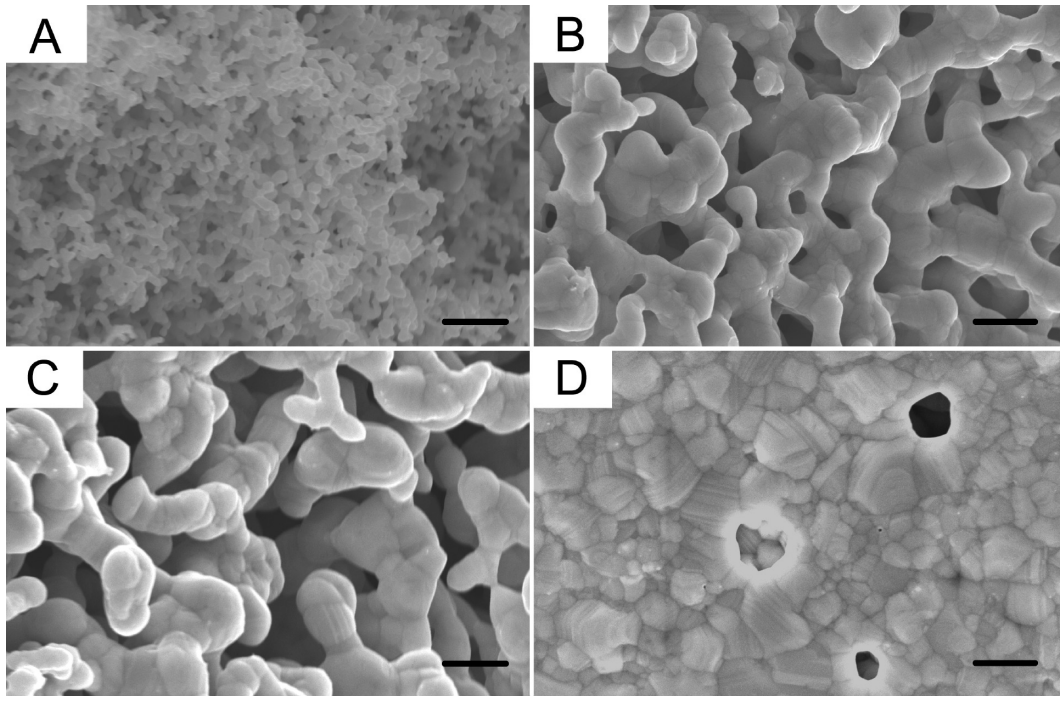


FIGURE 7. SEM images of the Ag nanoparticles synthesized by CCVC (a) without thermal treatment and after being isothermally heated at different temperatures for 5 min: (b) 230, (c) 250, and (d) 260 °C. Scale bars are 400 nm.

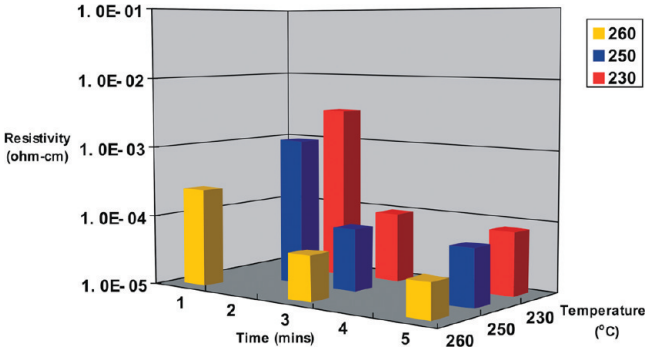


FIGURE 8. Effects of curing time and temperature on the resistivity of polymer nanocomposites.

the effect of curing (or sintering) time and temperature on the resistivity of polymer nanocomposites. When cured at 230 and 250 °C for 2 min or at 260 °C for 1 min, the polymer nanocomposites show high resistivities. When the curing time is 3 min, the polymer nanocomposites prepared at 230 °C show a lower resistivity ($9.8 \times 10^{-5}$ Ω cm) than those of conventional silver-filled polymer composites at the same filler loading. As the temperature increases, polymer nanocomposites with even lower resistivities can be obtained. Increasing curing time to 5 min led to a further decrease in electrical resistivity for the samples cured at 260 °C. This improvement in conductivity was less pronounced for the samples cured at 230 and 250 °C. Extending the curing time to 10 min at 260 °C results in the polymer nanocomposites with a resistivity of as low as about $6.0 \times 10^{-6}$ Ω cm, close to the resistivity of bulk silver. In addition, polymer nanocomposites cured using a typical lead-free solder reflow profiles show electrical resistivity of $6.3 \times 10^{-5}$ Ω cm. The preparation of highly conductive polymer nanocomposites during solder reflow reduces the processing steps and cost, enabling the natural integration into standard industrial electronic packaging processes.

Figure 9 shows the cross-section of polymer nanocomposites cured at 230, 250, and 260 °C for 5 min and 260 °C for 10 min. At 230 °C, the particles within the polymer matrix were connected to one another and formed necks (Figure 9a). At 250 °C, the neck size between the particles increased and rodlike structures formed (Figure 9b). When increasing the temperature to 260 °C, the particles grew significantly and necking was more prominent (Figure 9 (c)). When curing was conducted at 260 °C for 10 min, smoother facets with elongated particle structures formed (Figure 9d). The necking exhibited during the sintering process effectively reduces or even eliminates the contact resistance among the conductive fillers and enable the formation of 3D continuous conductive networks within the polymer matrix, leading to the highly conductive polymer nanocomposites.

**Rheological Properties and Noncontact Printing of the Paste.** The noncontact printing is defined as the accurate dispensing of materials onto a selective location without physical contact in a controlled manner. The attractive features of noncontact printing technologies are cost-effectiveness, reduced waste of precious materials, the accurate dispensing of a small amount of materials onto a selective location, no special requirements for substrates (e.g., roughness, flexibility), and environmental friendliness (60−62). Despite these advantages many of the necessary processing conditions are still not fully understood. Most importantly, the effect of the rheological properties of the printed materials on the printing process is still undetermined. The viscosity of any printed composite materials strongly depends on the filler loading, filler size, shape, and additives that are used to tune the rheological properties. Noncontact printing technologies

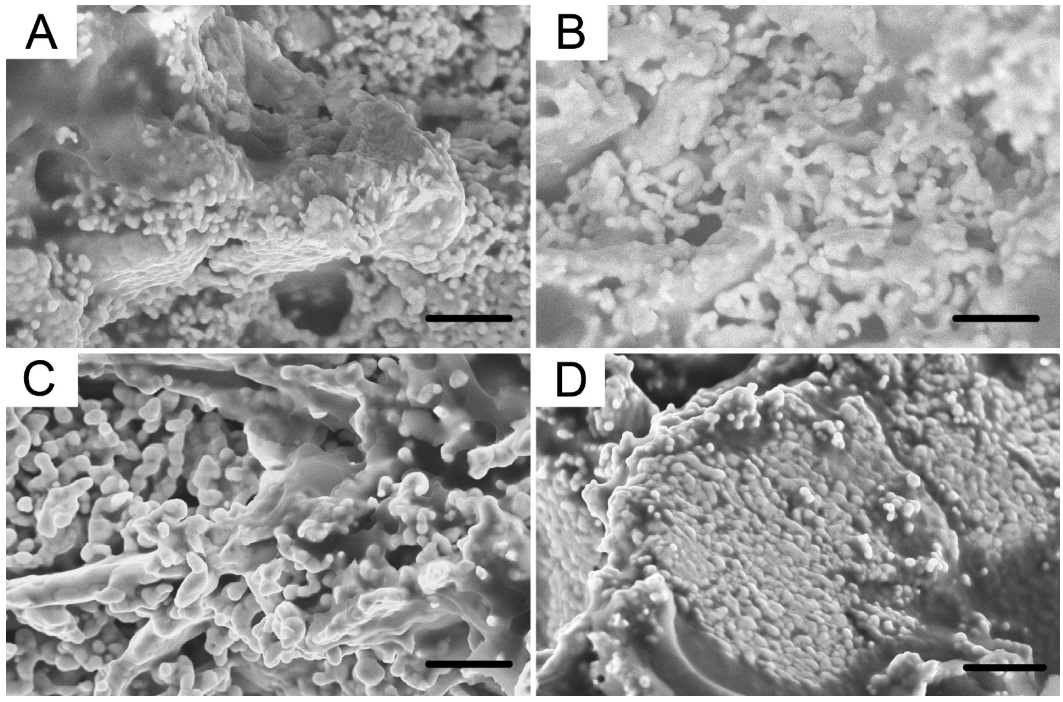


FIGURE 9. SEM images of the cross-section of polymer nanocomposites cured at (a) 230 °C, 5 min; (b) 250 °C, 5 min; (c)260 °C, 5 min; and (d)260 °C, 10 min. Scale bars are 2 $\mu$m.

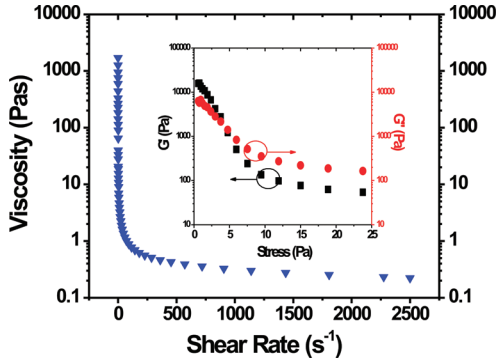


FIGURE 10. Viscosity as a function of shear rate for the paste filled with 80 wt % Ag fillers. Inset is an oscillatory stress sweep test for the paste.

require that the materials should readily flow and have the ability to recover its viscosity rapidly to retain the shape of the adhesive paste after printing (63). With the incorporation of silver nanoparticles, the viscosity of the conductive adhesive paste (the mixture of conductive fillers, the epoxy resin, etc., before curing) increases dramatically at low shear rates. However, the addition of large amounts of solvent to reduce the viscosity would result in the sedimentation of silver flakes, which causes variations in the local silver concentration and may block the nozzle (16). These requirements render noncontacting printing of highly viscous pastes challenging. Figure 10 shows the viscosity vs shear rate of the paste used in the present study. The paste showed a typical shear thinning behavior. The viscosity of the paste at a shear rate of 2500 $s^{-1}$ was 221 mPa s, much higher than that of typical silver inks (<40 mPa s). Note that polymers or polymer composites for inkjet printing must be diluted to meet the viscosity requirement (64). The shear thinning behavior of the paste is related to the trade-off between breakdown due to flow stresses and build-up due to in-flow collision and Brownian motion (65, 66). When no shear force is exerted on the paste, the particles aggregate because of attraction forces such as van der Waals force. Aggregation caused by these forces can promote the formation of spatial networks, which creates an internal structure. The internal structure is important to provide long-term dispersion stability (63). Under shear, the weak forces within the paste are broken and the paste is dispensed easily. To gain insights into the structure and measure the viscoelasticity of the paste, oscillatory stress sweep of the paste was performed, as shown in Figure 10 (inset). Storage modulus ($G'$) and loss modulus ($G''$) measured in the oscillatory test represent solid and liquid characteristics of the paste. At low shear stresses the pastes show a dominant solidlike behavior ($G' > G''$) and as the applied stress increases, the paste gradually changes from solidlike (elastic) behavior to liquidlike (viscous) behavior. The point at which $G' = G''$ is a solid−fluid transition and an indicator for assessing the cohesiveness of the paste (67). We have found that if the applied shear stress at the point where $G' = G''$ was too low, splashing occurred during the printing. In the present study, the applied stress was 4.37 Pa when $G'' = G''$, which was optimal for the noncontact printing.

Figure 11 shows the noncontact printing of the paste on the surfaces of glass (Figure 11A) and an silver-plating lead frame (Figure 11B−D). Depending on the interaction between the paste and substrates, the paste can either totally wet the glass surface with a radius of about 220 $\mu$m and a height of about 14.5 $\mu$m, or form a dot with a radius of 130 $\mu$m and a height of 49 $\mu$m on the silver-plating lead frame under optimized conditions. Following cure, because of the shrinkage of epoxy resins, the printed dots have a radius of 120 $\mu$m and a height of 28 $\mu$m. Generally, the Weber number ($We$), defined as the ratio of kinetic energy to the surface energy of a

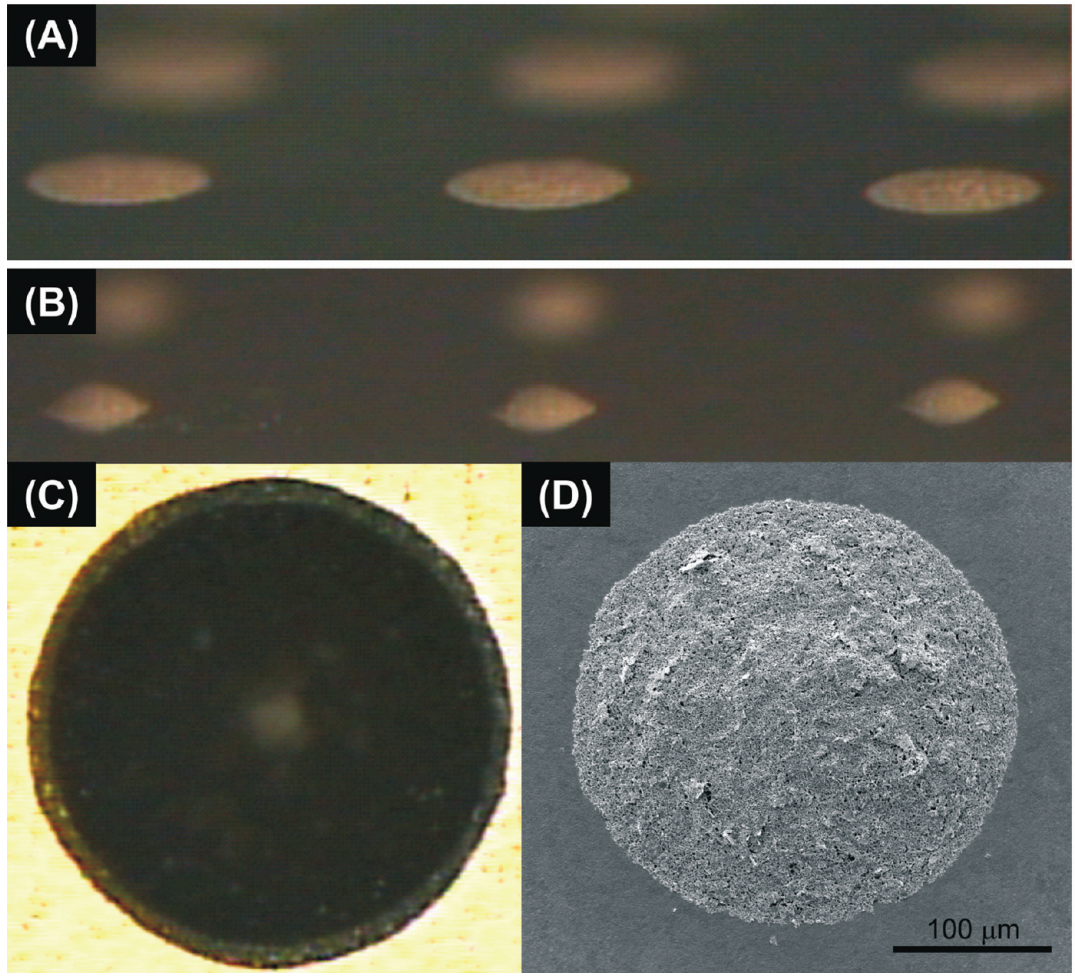


**FIGURE 11. Noncontact printing of the paste with 80 wt % Ag fillers on (A) a glass slide (side view, optical microscopy) with a radius of about 220 $\mu$m, (B) on an Ag-plating lead frame with a radius of 130 $\mu$m (side view, optical microscopy), (C) on an Ag-plated lead frame with a dot size (top view, microscopy) before curing, and (D) on an Ag-plated lead frame with a dot size (top view, SEM) after curing.**

droplet (eq 2), provides a good estimate whether the droplet has sufficient kinetic energy to overcome the surface tension at the orifice and to create a free flying droplet (68). There is a critical Weber number below which a free flying droplet cannot be created. For inviscid liquids, the critical Weber number is about 12 (eq 3); for printed materials whose viscosities are not negligible, the critical Weber number can be much larger than 12 and is related to the viscosity through the Ohnesorge number (*Oh*) (eq 4 and 5).

$$We = \frac{\rho D v^2}{\sigma} \tag{2}$$

$$We_{\text{critical}} \approx 12 \ (\eta \approx 0) \tag{3}$$

$$We_{\text{critical}} = 12 \times (1 + 1.07 Oh^{1.6}) \ (\eta > 0) \tag{4}$$

$$Oh = \frac{\eta}{\sqrt{\rho D \sigma}} \tag{5}$$

Where $\rho$ is the density, $v$ is the velocity, $D$ is the drop diameter before impact, $\sigma$ is the surface tension, and $\eta$ is the dynamic viscosity. Increasing the viscosity of the printed materials leads to an increase in Ohnesorge number and a dramatic increase in the critical Weber number, making the creation of small droplets from viscous materials very difficult (68). To the best of our knowledge, this is the first successful attempt to print highly viscous adhesive pastes into dot arrays with such a small size on the substrate in the open literature. The noncontact printing of the highly viscous adhesive opens up new avenues for low-cost printed electronics. Increased understanding of the correlation between the rheological properties and the noncontact printing process is needed to optimize material and printing parameters to obtain ultrahigh resolution noncontact printing technologies for low cost interconnects of the future.

## 4. CONCLUSIONS

We have demonstrated the fast preparation of printable highly conductive polymer nanocomposites using thermal decomposition of silver carboxylate on the surface of silver flakes and sintering between conductive fillers during the adhesive curing process. The sintering between conductive fillers effectively reduces or even eliminates the contact resistance, leading to polymer nanocomposites with the electrical resistivities of $8.1 \times 10^{-5}$, $6.0 \times 10^{-6}$, and $6.3 \times 10^{-5}$ $\Omega$ cm when prepared at 230 °C for 5 min, at 260 °C for 10 min, and using a typical lead-free solder reflow

process, respectively. By optimizing the rheological properties, we have demonstrated that the highly viscous adhesive pastes can be noncontact printed into a microarray of dots with a radius of 130 $\mu$m. The polymer nanocomposites with superior electrical conductivity and fast processing along with noncontact printing technologies will considerably reduce the cost of interconnection in printed electronics, enabling their wide scale industrial application.

**Acknowledgment.** We thank Nokia and U.S. National Science Foundation (CMMI 0621115) for the financial support, ASM Pacific Technology Ltd. for the noncontact printing tests of the materials, nGimat for silver nanoparticles, Ferro Corp. for silver flakes, and Lindau Chemical Corp. for the anhydride. We thank David Lu, Wenbin Xu, Hongjin Jiang, Yonghao Xiu, and Josh C. Agar for their helpful discussion.

## REFERENCES AND NOTES

(1) Li, Y.; Moon, K.-S.; Wong, C. P. *Science* **2005**, *308*, 1419–1420.
(2) Li, Y.; Wong, C. P. *Mater. Sci. Eng., R* **2006**, *R51*, 1–35.
(3) Chun, S.; Grudinin, D.; Lee, D.; Kim, S.-H.; Yi, G.-R.; Hwang, I. *Chem. Mater.* **2009**, *21*, 343–350.
(4) Pulkkinen, P.; Shan, J.; Leppanen, K.; Kansakoski, A.; Laiho, A.; Jarn, M.; Tenhu, H. *ACS Appl. Mater. Interfaces* **2009**, *1*, 519–525.
(5) Zhang, R.; Lin, W.; Lawrence, K.; Wong, C. P. *Int. J. Adhes. Adhes.* **2010**, *30*, 403–407.
(6) Perelaer, J.; de Laat, A. W. M.; Hendriks, C. E.; Schubert, U. S. *J. Mater. Chem.* **2008**, *18*, 3209–3215.
(7) Van Osch, T. H. J.; Perelaer, J.; de Laat, A. W. M.; Schubert, U. S. *Adv. Mater.* **2008**, *20*, 343–345.
(8) Woo, K.; Kim, D.; Kim, J. S.; Lim, S.; Moon, J. *Langmuir* **2009**, *25*, 429–433.
(9) Magdassi, S.; Bassa, A.; Vinetsky, Y.; Kamyshny, A. *Chem. Mater.* **2003**, *15*, 2208–2217.
(10) Perelaer, J.; Klokkenburg, M.; Hendriks, C. E.; Schubert, U. S. *Adv. Mater.* **2009**, *21*, 4830–4834.
(11) Dearden, A. L.; Smith, P. J.; Shin, D.-Y.; Reis, N.; Derby, B.; O'Brien, P. *Macromol. Rapid Commun.* **2005**, *26*, 315–318.
(12) Gamerith, S.; Klug, A.; Scheiber, H.; Scherf, U.; Moderegger, E.; List, E. J. W. *Adv. Funct. Mater.* **2007**, *17*, 3111–3118.
(13) Calvert, P. *Chem. Mater.* **2001**, *13*, 3299–3305.
(14) Singh, M.; Haverinen, H. M.; Dhagat, P.; Jabbour, G. E. *Adv. Mater.* **2010**, *22*, 673–685.
(15) Chabinyc, M. L.; Salleo, A. *Chem. Mater.* **2004**, *16*, 4509–4521.
(16) Kolbe, J.; Arp, A.; Calderone, F.; Meyer, E. M.; Meyer, W.; Schaefer, H.; Stuve, M. *Microelectron. Reliab.* **2007**, *47*, 331–334.
(17) Jang, D.; Kim, D.; Lee, B.; Kim, S.; Kang, M.; Min, D.; Moon, J. *Adv. Funct. Mater.* **2008**, *18*, 2862–2868.
(18) Fuller, S. B.; Wilhelm, E. J.; Jacobson, J. M. *J. Microelectromech. Syst.* **2002**, *11*, 54–60.
(19) Okada, I.; Shimoda, K. US Patent 7608203 2009.
(20) Chung, K.-c.; Cho, H.-n.; Gong, M.-s.; Han, Y.-s.; Jeong-bin, P.; Nam, D.-h.; Uhm, S.-y.; Seo, Y.-k.; Cho, N.-b. U.S. Patent Application 2008/0206488.
(21) Jiang, H.; Moon, K.-S.; Li, Y.; Wong, C. P. *Chem. Mater.* **2006**, *18*, 2969–2973.
(22) Lu, D. D.; Li, Y. G.; Wong, C. P. *J. Adhes. Sci. Technol.* **2008**, *22*, 815–834.
(23) Zhang, R.; Moon, K.-S.; Lin, W.; Wong, C. P. *J. Mater. Chem.* **2010**, *20*, 2018–2023.
(24) Hunt, A. T.; Carter, W. B.; Cochran, J. K. *Appl. Phys. Lett.* **1993**, *63*, 266–268.
(25) Oljaca, M.; Xing, Y.; Lovelace, C.; Shanmugham, S.; Hunt, A. *J. Mater. Sci. Lett.* **2002**, *21*, 621–626.
(26) Stark, W. J.; Maedler, L.; Maciejewski, M.; Pratsinis, S. E.; Baiker, A. *Chem. Commun.* **2003**, 588–589.
(27) Lu, D.; Wong, C. P. *J. Therm. Anal. Calorim.* **2000**, *59*, 729–740.
(28) Lu, D.; Wong, C. P. *J. Therm. Anal. Calorim.* **2000**, *61*, 3–12.
(29) Miragliotta, J.; Benson, R. C.; Phillips, T. E. *Mater. Res. Soc. Symp. Proc.* **1997**, *445*, 217–222.
(30) Markley, D. L.; Tong, Q. K.; Magliocca, D. J.; Hahn, T. D. *Proceedings of the International Symposium on Advanced Packaging Materials: Processes, Properties and Interfaces*; Braselton, GA, March 14–17, 1997; IEEE: Piscataway, NJ, 1999; pp 16–20.
(31) Yamamoto, S.; Fujiwara, K.; Watarai, H. *Anal. Sci.* **2004**, *20*, 1347–1352.
(32) Moskovits, M.; Suh, J. S. *J. Am. Chem. Soc.* **1985**, *107*, 6826–6829.
(33) Ishioka, T.; Wakisaka, H.; Saito, T.; Kanesaka, I. *Spectrochim. Acta, Part A* **2001**, *57A*, 129–135.
(34) Waterhouse, G. I. N.; Bowmaker, G. A.; Metson, J. B. *Phys. Chem. Chem. Phys.* **2001**, *3*, 3838–3845.
(35) Abe, K.; Hanada, T.; Yoshida, Y.; Tanigaki, N.; Takiguchi, H.; Nagasawa, H.; Nakamoto, M.; Yamaguchi, T.; Yase, K. *Thin Solid Films* **1998**, *327–329*, 524–527.
(36) Lee, S. J.; Kim, K. *Chem. Commun.* **2003**, 212–213.
(37) Lee, S. J.; Han, S. W.; Choi, H. J.; Kim, K. *J. Phys. Chem. B* **2002**, *106*, 2892–2900.
(38) Yang, N.; Aoki, K.; Nagasawa, H. *J. Phys. Chem. B* **2004**, *108*, 15027–15032.
(39) Uvarov, N. F.; Burleva, L. P.; Mizen, M. B.; Whitcomb, D. R.; Zou, C. *Solid State Ionics* **1998**, *107*, 31–40.
(40) Liu, X.; Lu, S.; Zhang, J.; Cao, W. *Thermochim. Acta* **2006**, *440*, 1–6.
(41) Greer, J. R.; Street, R. A. *Acta Mater.* **2007**, *55*, 6345–6349.
(42) Moon, K.-S.; Dong, H.; Maric, R.; Pothukuchi, S.; Hunt, A.; Li, Y.; Wong, C. P. *J. Electron. Mater.* **2005**, *34*, 168–175.
(43) Ide, E.; Angata, S.; Hirose, A.; Kobayashi, K. F. *Acta Mater.* **2005**, *53*, 2385–2393.
(44) Chen, M.; Wang, L.-Y.; Han, J.-T.; Zhang, J.-Y.; Li, Z.-Y.; Qian, D.-J. *J. Phys. Chem. B* **2006**, *110*, 11224–11231.
(45) Washio, I.; Xiong, Y.; Yin, Y.; Xia, Y. *Adv. Mater.* **2006**, *18*, 1745–1749.
(46) Zhou, Y.; Yu, S. H.; Wang, C. Y.; Li, X. G.; Zhu, Y. R.; Chen, Z. Y. *Adv. Mater.* **1999**, *11*, 850–852.
(47) Yamamoto, M.; Nakamoto, M. *J. Mater. Chem.* **2003**, *13*, 2064–2065.
(48) Yamamoto, M.; Kashiwagi, Y.; Nakamoto, M. *Langmuir* **2006**, *22*, 8581–8586.
(49) Kotthaus, S.; Guenther, B. H.; Haug, R.; Schaefer, H. *IEEE Trans. Compon., Packag., Manuf. Technol., Part A* **1997**, *20*, 15–20.
(50) Dong, T.-Y.; Chen, W.-T.; Wang, C.-W.; Chen, C.-P.; Chen, C.-N.; Lin, M.-C.; Song, J.-M.; Chen, I.-G.; Kao, T.-H. *Phys. Chem. Chem. Phys.* **2009**, *11*, 6269–6275.
(51) Nguyen, B. T.; Gautrot, J. E.; Nguyen, M. T.; Zhu, X. X. *J. Mater. Chem.* **2007**, *17*, 1725–1730.
(52) Oljaca, M.; Maric, R.; Shanmugham, S.; Hunt, A. *Am. Ceram. Soc. Bull.* **2003**, *82*, 38–40.
(53) Zhang, R.; Zhang, D.; Mao, H.; Song, W.; Gao, G.; Liu, F. *J. Mater. Res.* **2006**, *21*, 349–354.
(54) Kolobov, A. V.; Rogalev, A.; Wilhelm, F.; Jaouen, N.; Shima, T.; Tominaga, J. *Appl. Phys. Lett.* **2004**, *84*, 1641–1643.
(55) Anto, B. T.; Sivaramakrishnan, S.; Chua, L.-L.; Ho, P. K. H. *Adv. Funct. Mater.* **2010**, *20*, 296–303.
(56) Ye, L.; Lai, Z.; Liu, J.; Tholen, A. *IEEE Trans. Electron. Packag. Manuf.* **1999**, *22*, 299–302.
(57) Lee, H.-H.; Chou, K.-S.; Shih, Z.-W. *Int. J. Adhes. Adhes.* **2005**, *25*, 437–441.
(58) Bai, J. G.; Lei, T. G.; Calata, J. N.; Lu, G.-Q. *J. Mater. Res.* **2007**, *22*, 3494–3500.
(59) Untereker, D.; Lyu, S.; Schley, J.; Martinez, G.; Lohstreter, L. *ACS Appl. Mater. Interfaces* **2009**, *1*, 97–101.
(60) Kamyshny, A.; Ben-Moshe, M.; Aviezer, S.; Magdassi, S. *Macromol. Rapid Commun.* **2005**, *26*, 281–288.
(61) Cheng, K.; Yang, M.-H.; Chiu, W. W. W.; Huang, C.-Y.; Chang, J.; Ying, T.-F.; Yang, Y. *Macromol. Rapid Commun.* **2005**, *26*, 247–264.
(62) Tekin, E.; Smith, P. J.; Schubert, U. S. *Soft Matter* **2008**, *4*, 703–713.
(63) Bell, G. C.; Rosell, C. M.; Joslin, S. T. *IEEE Trans. Compon., Hybrids, Manuf. Technol.* **1987**, *10*, 507–510.
(64) De Gans, B.-J.; Duineveld, P. C.; Schubert, U. S. *Adv. Mater.* **2004**, *16*, 203–213.
(65) Barnes, H. A. *J. Non-Newtonian Fluid Mech.* **1997**, *70*, 1–33.
(66) Durairaj, R.; Ekere, N. N.; Salam, B. *J. Mater. Sci.: Mater. Electron.* **2004**, *15*, 677–683.
(67) Durairaj, R.; Mallik, S.; Seman, A.; Marks, A.; Ekere, N. N. *J. Mater. Process. Technol* **2009**, *209*, 3923–3930.
(68) Koltay, P.; Zengerle, R. *Digest of Technical Papesr of the 14th International Conference on Solid-State Sensors, Actuators and Microsystems*; Lyon, France, June 10–14, 2007; pp 165–170.

AM100456M